UCSF

Title
Chemically induced vesiculation as a platform for studying TMEM16F activity

Permalink
https://escholarship.org/uc/item/1gq7v9k3

Journal
Proceedings of the National Academy of Sciences of the United States of America, 116(4)

ISSN
0027-8424

Authors
Han, Tina W
Ye, Wenlei
Bethel, Neville P
et al.

Publication Date
2019-01-22

DOI
10.1073/pnas.1817498116

Peer reviewed

Chemically induced vesiculation as a platform for studying TMEM16F activity

Tina W. Han[a,b,c], Wenlei Ye[a,b,c,1], Neville P. Bethel[d,1], Mario Zubia[a,b,c], Andrew Kim[a,b,c], Kathy H. Li[e], Alma L. Burlingame[e], Michael Grabe[d], Yuh Nung Jan[a,b,c], and Lily Y. Jan[a,b,c,2]

[a]Howard Hughes Medical Institute, University of California, San Francisco, CA 94143; [b]Department of Physiology, University of California, San Francisco, CA 94143; [c]Department of Biochemistry and Biophysics, University of California, San Francisco, CA 94143; [d]Department of Pharmaceutical Chemistry, Cardiovascular Research Institute, University of California, San Francisco, CA 94143; and [e]Mass Spectrometry Facility, University of California, San Francisco, CA 94143

Calcium-activated phospholipid scramblase mediates the energy-independent bidirectional translocation of lipids across the bilayer, leading to transient or, in the case of apoptotic scrambling, sustained collapse of membrane asymmetry. Cells lacking TMEM16F-dependent lipid scrambling activity are deficient in generation of extracellular vesicles (EVs) that shed from the plasma membrane in a Ca^{2+}-dependent manner, namely microvesicles. We have adapted chemical induction of giant plasma membrane vesicles (GPMVs), which require both TMEM16F-dependent phospholipid scrambling and calcium influx, as a kinetic assay to investigate the mechanism of TMEM16F activity. Using the GPMV assay, we identify and characterize both inactivating and activating mutants that elucidate the mechanism for TMEM16F activation and facilitate further investigation of TMEM16F-mediated lipid translocation and its role in extracellular vesiculation.

TMEM16F | phospholipid scrambling | extracellular vesicles | calcium influx | GPMV

Cellular membranes are composed of asymmetrically partitioned lipids such that certain species are sequestered to the inner leaflet while others are exposed on the outer leaflet. Lipid asymmetry is established and maintained by ATP-dependent unidirectional phospholipid translocases which are colloquially referred to as "flippases" and "floppases" (1–3). A third class of proteins, aptly called "scramblases," mediates bidirectional translocation of lipids across the bilayer in a Ca^{2+}-activated, energy-independent manner, which leads to a transient or, in the case of apoptotic scrambling, sustained collapse of membrane asymmetry (2, 4, 5). Lipid scrambling is activated in platelets during blood coagulation, resulting in the cell surface exposure of phosphatidylserine (PS), a negatively charged aminophospholipid normally sequestered on the inner leaflet of the lipid bilayer under resting conditions (6). PS externalization provides binding sites for the assembly of factor Xa and factor Va, which work together to catalyze the conversion of prothrombin to thrombin, an essential intermediary in the blood coagulation cascade (7).

Patients diagnosed with a bleeding disorder called Scott syndrome have platelets that are defective in lipid scrambling (8). The molecular identity of the scramblase remained elusive until Scott patients were discovered to harbor exon splice site mutations in the TMEM16F gene resulting in premature termination of mRNA translation (9, 10). TMEM16F, also known as anoctamin-6 or Ano6, is a member of the TMEM16 family of 10 transmembrane segment-containing proteins that are capable of forming homodimers with each monomer subunit coordinating two Ca^{2+} ions (11–13). This family includes founding member TMEM16A and closely related paralog TMEM16B, which are calcium-activated chloride channels (14, 15). By contrast, TMEM16F has been characterized as a small-conductance Ca^{2+}-activated nonselective cation channel (16, 17). TMEM16F knockout mice reliably recapitulate the blood coagulation deficiencies observed in Scott patients (16, 18). Furthermore, dogs with a hereditary bleeding disorder similar to Scott syndrome also exhibit mutations in the

TMEM16F gene leading to loss of protein function (19). In addition to TMEM16F, five other members of the mammalian TMEM16 family have been attributed with phospholipid scrambling activity: TMEM16C, TMEM16D, TMEM16E, TMEM16G, and TMEM16J (20, 21). Furthermore, lipid scrambling activity is exhibited by fungal TMEM16 homologs from *Nectria haematococca* and *Aspergillus fumigatus* that are reconstituted into liposomes (11, 22) and mouse TMEM16F isolated in a lipid bilayer microarray (23), suggesting that TMEM16 proteins may be directly responsible for scramblase activity.

Cells lacking TMEM16F-mediated lipid scrambling activity are also deficient in microvesicle generation in humans (8, 24) and in mice (18, 25, 26), although it is not well understood how scrambling relates to vesiculation. Microvesicles are a subset of extracellular vesicles (EVs) that have also been referred to as "microparticles" or "ectosomes" in the literature. They distinctively shed from the plasma membrane in a Ca^{2+}-dependent manner and range in size from 100 nm to 1 μm in diameter depending on the cell type of origin (27, 28). EVs are thought to carry bioactive cargo in the form of RNAs, proteins, and/or lipids which can elicit biological activity in other cells in either a short-range or long-range manner (27, 28). Platelet microvesicles are one of the earliest reported examples of EVs; they were first biochemically purified as procoagulation activity in a cell-free fraction (29) and then demonstrated by electron microscopy to be membrane-bound vesicles (30). TMEM16F-dependent EVs have also been implicated in the anti-inflammatory properties of neutrophils in joint inflammation (26), mineral deposition

---

Significance

Extracellular vesicles, which are released from cells via budding of the cell membrane and may carry bioactive cargo such as RNAs and proteins, can elicit biological activity in other cells in a short-range or long-range manner. Extracellular vesicles that depend on TMEM16F activity for their formation play important roles in blood coagulation, mineral deposition during bone development, and protection of the joint in inflammatory arthritis. This study employs a newly developed kinetic assay to investigate the TMEM16F protein functions that are involved in extracellular vesicle formation, such as TMEM16F-dependent calcium influx and TMEM16F-dependent phospholipid scrambling.

---

during bone development (25), and modulating T cell receptor signaling (31, 32).

Quantification of extracellular vesicles using conventional techniques is challenging due to the inherent difficulties of resolving particles on a nanoscale. Here we use chemically induced giant plasma membrane vesicles (GPMVs) to investigate the role of TMEM16F phospholipid scrambling activity in extracellular vesiculation. Due to their enlarged dimensions, GPMVs can be monitored in real time by conventional light microscopy, revealing that vesiculation depends on TMEM16F-mediated lipid scrambling and vesicle formation begins after the initiation of PS exposure. Strikingly, we find these giant vesicles to robustly depend on Ca^{2+} activation of TMEM16F and TMEM16F-dependent Ca^{2+} entry. Using the GPMV assay, we identify and characterize both inactivating and activating TMEM16F mutants in kinetic analyses that facilitate further investigation of TMEM16F-mediated lipid translocation and extracellular vesicle formation.

Results

TMEM16F-Deficient Cells Have Impaired Ability to Generate GPMVs.
GPMVs are chemically induced to form blebs from cultured cells using sulfhydryl blocking reagents such as formaldehyde, N-ethylmaleimide, and iodoacetamide (33, 34). Similar to microvesicles, they are shed from the plasma membrane, are dependent on calcium, and expose PS on the vesicle surface (33–35). More recently, GPMVs have been demonstrated to segregate into micrometer-scale lipid raft-like domains and have proven useful for the study of membrane phase separation (36, 37).

To assess whether the GPMV assay could be used as a tool for studying the role of TMEM16F in vesiculation, we first asked whether production of these giant vesicles was dependent on expression of the TMEM16F protein. We cultured primary mouse embryonic fibroblasts (MEFs) from wild-type (WT), TMEM16F heterozygotes (16F^{Het}), and knockout (16F^{KO}) mouse embryos and induced vesiculation using extracellular solution containing 25 mM paraformaldehyde (PFA), 2 mM DTT, and 2 mM $CaCl_2$. WT MEFs robustly produced GPMVs which terminated production about 60 min posttreatment; by contrast, 16F^{Het} and 16F^{KO} MEFs exhibited resistance to GPMV formation posttreatment (Fig. 1A and Movies S1–S3). We did not observe vesicles produced by 16F^{Het} cells until 90 min posttreatment, and the vesicle diameter was smaller than that of WT. The 16F^{KO} cells completely failed to vesiculate within the time allotted for the experiment. Western blot analysis indicated that 16F^{Het} MEFs express TMEM16F protein at about 50% of the normal level and confirmed that 16F^{KO} MEFs lack TMEM16F expression (Fig. 1B).
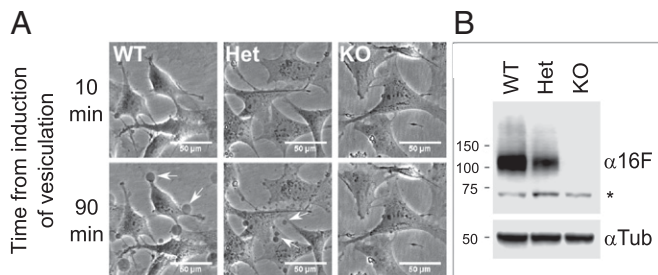
Fig. 1. TMEM16F-deficient MEF cells show impaired GPMV generation. (A) Wild type (WT), TMEM16F^{Het} (Het), and TMEM16F^{KO} (KO) primary MEFs are treated with 25 mM PFA and 2 mM DTT in a 2-mM Ca^{2+} buffer to induce GPMVs. WT MEFs show robust vesiculation after 90 min of treatment (white arrows), while TMEM16F^{Het} MEFs exhibit a diminished vesiculation response. TMEM16F^{KO} MEFs do not yield GPMVs within 90 min. (Scale bars: 50 μm.) (B) Western blot analysis of endogenous TMEM16F protein expression in WT and TMEM16F-deficient cells. The asterisk (*) denotes a nonspecific band; α16F, α-TMEM16F; α-Tub, α-tubulin.

Next, we performed proteomics to compare the protein compositions of GPMVs and microvesicles. In addition to primary MEF cells, GPMVs were successfully induced in many cell types, including microglial cell line BV2 and melanoma cells B16F10 but not HEK293 cells (SI Appendix, Fig. S1A). We performed shotgun proteomic experiments to identify proteins found in GPMVs isolated from three mouse cell lines (primary MEFs, B16F10, and BV2) as well as microvesicles purified from calcium ionophore activated mouse platelets (SI Appendix, Fig. S1B and Dataset S1). We found 750 proteins that were in common among the three GPMV samples, representing 56, 53, and 73% of total proteins assigned in MEF, B16F10, and BV2 GPMVs, respectively. Of these shared GPMV proteins, 191 proteins were also found to be in common with proteins identified from platelet microvesicles. We reasoned that this overlapping set of proteins among all four EV samples might represent a core complement of proteins required for EV biogenesis regardless of the cell type of origin. Using the gene ontology term "extracellular exosome" (GO: 0070062), we generated a list of 2,620 EV-related genes in the mouse genome and converted the mouse genome informatics (MGI) identifiers to 10,802 UniProtKB IDs. Of the 191 proteins found in common from extracellular vesicles of all four cell types, 167 (or 87%) were annotated as potential EV proteins. This is a fourfold enrichment over the expected baseline percentage of 21% (10,802 out of 51,434 total proteins in the UniProt database, February 2018) and has a two-tailed P value of <0.0001 calculated using a χ^2 test with Yates correction. Because GPMVs resemble microvesicles not only in their dependence on calcium and TMEM16F but also in their protein composition, we next tested whether TMEM16F expression in HEK293 cells can confer the ability of GPMV formation to establish a platform for assessing the dependence of EV formation on various aspects of TMEM16F functions in mutagenesis studies.

Overexpression of TMEM16F in HEK293 Cells Confers Ability to Produce GPMVs. Having found that HEK293 cells exhibited resistance to vesiculation, we performed Western blot and observed that HEK293 cells expressed much lower levels of endogenous TMEM16F protein than GPMV-competent cell types (SI Appendix, Fig. S1C). To test whether overexpression of TMEM16F in HEK293 cells might confer the ability of HEK293 cells to respond to chemically induced vesiculation, we used lentivirus to generate a stable HEK293 cell line that expressed mouse TMEM16F tagged on the C terminus with mCherry (16F-mCh). TMEM16F expression in these cells is localized primarily to the plasma membrane, whereas the control cell line, expressing cytoplasmic mCherry (mCh-cyto), showed diffuse mCherry signal in the cytosol (Fig. 2A). Because mCh-cyto fluoresces brighter under the microscope than 16F-mCh, we expressed it using a weaker PGK promoter, which led to ~20-fold less protein expression than 16F-mCh driven by a CMV promoter. Such discrepancy in protein expression level is reflected in the Western blot analysis using an mCherry antibody, whereby longer exposure time is needed to detect the mCh-cyto signal than that of 16F-mCh regardless of their comparable fluorescence signals visualized under microscopy (Fig. 2B). Overexpression of TMEM16F was indeed capable of conferring the ability to generate GPMVs to previously unresponsive HEK293 cells (Top Row in Fig. 2C and Movie S4). By contrast, mCh-cyto cells remained resistant to GPMV induction (Bottom Row in Fig. 2C and Movie S5), a condition similar to untransfected HEK293 cells. From these time-lapse images, we quantified GPMV production by 16F cells using an edge detection algorithm to count newly formed vesicles (SI Appendix, Fig. S2) and observed that the increase in GPMVs with time was sigmoidal (Fig. 2D), with a delay in GPMV onset of 24.2 ± 0.6 min, a growth phase of GPMV formation lasting 14.2 ± 0.2 min with a maximum vesiculation rate (V_{max}) of 0.1 ± 0.01 GPMVs per cell/min, and a termination in GPMV formation after 38.3 ± 0.6 min resulting in an average of 2.3 ± 0.2 GPMVs formed per cell (Fig. 2E). Time of
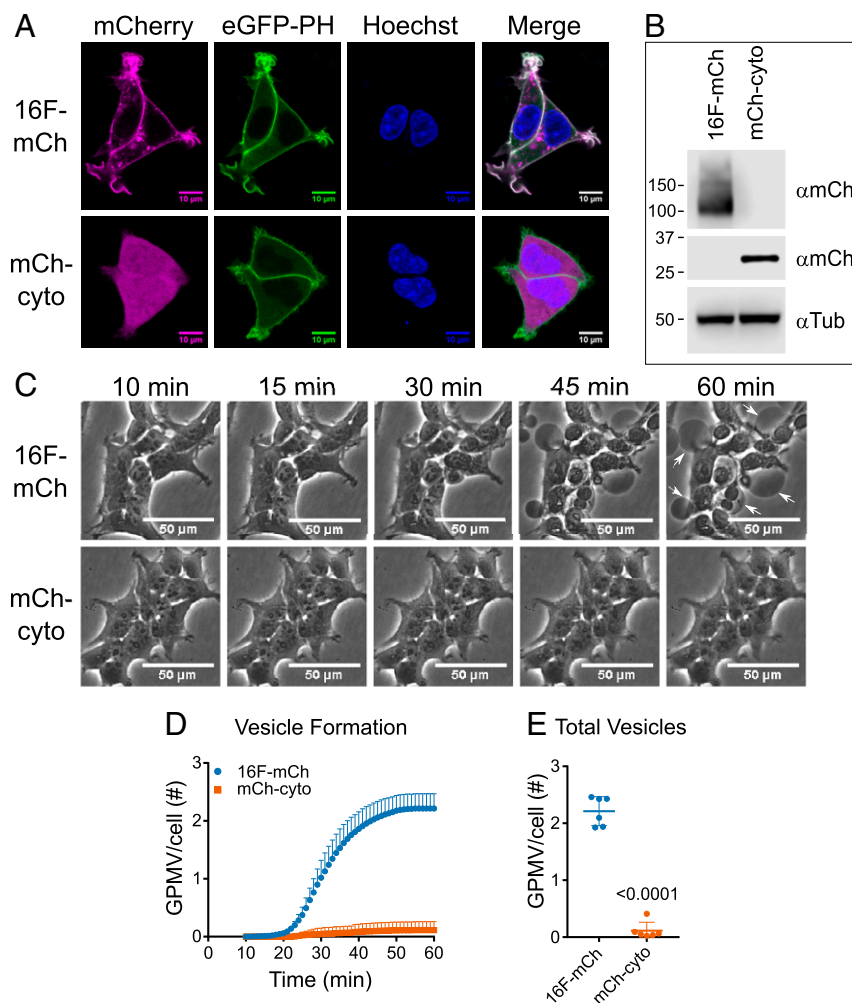
Fig. 2. TMEM16F overexpression endows HEK293 cells with the capacity for GPMV generation. (*A*) Exogenously expressed TMEM16F-mCherry (16F) is primarily localized to the plasma membrane and it colocalizes with eGFP-PH-PLCδ, a genetically encoded phosphatidylinositol-(4, 5)-bisphosphate (PIP$_2$) sensor used to demarcate the cell membrane. (*B*) Western blot analysis showing the level of TMEM16F-mCherry (16F) and mCh-cyto overexpression in HEK293 stable cell lines. Different exposure times are displayed for 16F and mCh-cyto bands due to disparate protein levels. (*C*) HEK293 cells stably expressing either TMEM16F-mCherry (16F-mCh) or mCh-cyto are chemically induced to generate GPMVs. GPMV generation is robustly induced in 16F-mCh cells (white arrows, *Top Row*), but mCh-cyto cells show no sign of vesiculation after 60 min of treatment (*Bottom Row*). (*D*) Quantification of GPMV generation during 1-h time course. (*E*) Average number of vesicles counted per cell after 1 h of GPMV induction. $P < 0.0001$ by unpaired two-tailed *t* test. (Scale bars: *A*, 10 μm; *C*, 50 μm.)

onset, V_{max}, and duration could not be determined for mCh-cyto cells since they do not visibly vesiculate within the allotted time.

GPMV Generation Depends on TMEM16F-Mediated Lipid Scrambling Activity. Having found that TMEM16F was required for the generation of GPMVs and sufficient to restore vesiculation to HEK293 cells, we wondered whether this was due to TMEM16F-dependent lipid scrambling activity. Through analysis of divergent sequences between TMEM16F (16F) and its nonscrambling paralog TMEMF16A (16A), a stretch of 35 amino acids [scrambling domain (SCRD)] was identified in TMEM16F that appeared to confer scrambling activity to TMEM16A when analogous residues were swapped (38). We wondered whether the scrambling-competent "AFA" chimera, a TMEM16A protein harboring the TMEM16F SCRD, could recapitulate the ability of TMEM16F to produce GPMVs in HEK293 cells and, likewise, whether the scrambling-deficient "FAF" chimera, which harbors the reciprocal swap in TMEM16F, and the nonscrambling TMEM16A would exhibit deficits in vesiculation. We generated stable HEK293 cell lines expressing the AFA chimera, the FAF chimera, and TMEM16A tagged with C-terminal mCherry. Consistent with our hypothesis that GPMV generation

was dependent on lipid scrambling, AFA expression was indeed able to confer vesiculation capability to HEK293 cells with no significant delay (Fig. 3 *A* and *D*), although reaching a diminished magnitude compared with 16F cells, producing on average 0.8 ± 0.2 vesicle per cell (Fig. 3*B*), and at a slower maximal rate, about 20% relative to 16F (Fig. 3*C*). By contrast, stable cell lines expressing the scrambling-deficient FAF or the nonscrambling 16A failed to vesiculate, similar to mCh-cyto and untransfected HEK293 cell lines.

Next, we verified that GPMV treatment induced lipid scrambling. It has been previously shown that PFA induces PS exposure in platelets (39), a cell type where TMEM16F-dependent vesiculation has been extensively characterized, and HeLa-P4 cells (40). We used pSIVA, an annexin-based reagent that fluoresces when bound to externalized PS, to indicate activation of lipid scrambling. Indeed, PS exposure is robustly induced in both 16F cells (Fig. 3*E*, *First Row*) and AFA cells (Fig. 3*E*, *Third Row*). By contrast, application of PFA fails to expose PS in cells expressing nonscrambling 16A (Fig. 3*E*, *Second Row*) and mCh-cyto cells (Fig. 3*E*, *Fifth Row*). As expected, FAF cells are defective in PFA-induced scrambling (Fig. 3*E*, *Fourth Row*); however, the expression of this chimera construct is weak on the
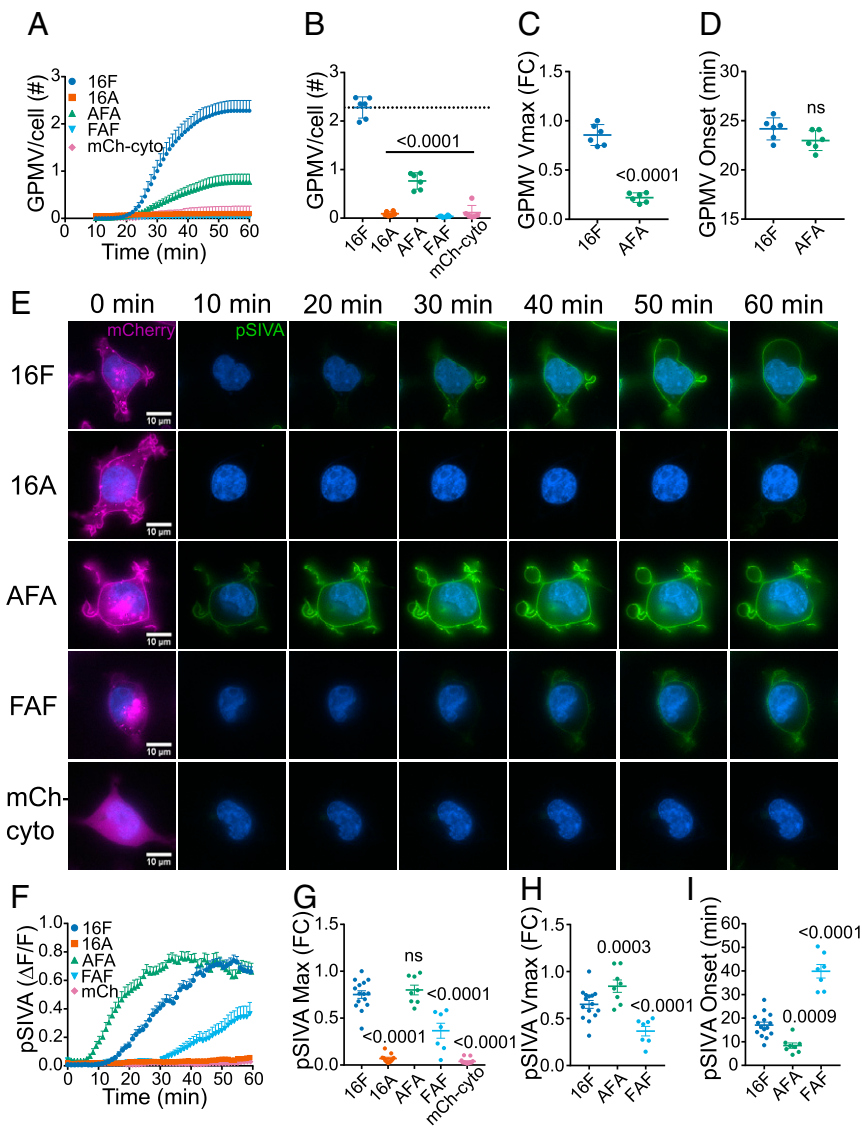
Fig. 3. GPMV generation requires TMEM16F-mediated lipid scrambling. (*A*) Quantification of the average number of GPMVs generated per cell over a time-lapse series. Scatter dot plots showing (*B*) the average number of GPMVs generated per cell by each cell line after 1 h of incubation, (*C*) maximum rate of vesiculation expressed as fold change relative to 16F, and (*D*) onset of GPMV formation. (*E*) Stable cell lines expressing wild-type TMEM16F-mCherry (16F), wild-type TMEM16A-mCherry (16A), TMEM16F::TMEM16A chimeras (AFA and FAF), and mCh-cyto are chemically induced to vesiculate for 1 h in the presence of pSIVA, a polarity-sensitive fluorescent PS binding reagent. At 0 min, cells are depicted as an overlay of mCherry (magenta), pSIVA (green), and Hoechst nuclear stain (blue). For all other time points, the mCherry channel is omitted for clarity. Representative images are shown. (Scale bars: 10 μm.) (*F*) Quantification of pSIVA fluorescence normalized to mCherry signal per cell over a time-lapse series. Scatter dot plots showing (*G*) the maximal pSIVA signal per cell expressed as fold change (FC) relative to 16F, (*H*) V_{max} of pSIVA accumulation, and (*I*) onset of pSIVA fluorescence. Statistical significance of all mutants compared with 16F wild type determined by one-way ANOVA followed by a Holm–Šídák multiple comparisons test for *B*, *G*, *H*, and *I*. Statistical significance was determined by an unpaired two-tailed *t* test for *C* and *D*; ns, not significant.

plasma membrane compared with 16F and AFA, so the resulting deficiency may be an overestimation. Quantification of average pSIVA fluorescence over the 1-h time course (Fig. 3*F*) reveals that although AFA cells achieve a maximal level of pSIVA fluorescence similar to that of 16F cells (Fig. 3*G*), they appear to scramble at a faster rate (Fig. 3*H*) and have an onset time of 8.4 ± 3.2 min after stimulation, which is about 10 min faster than 16F scrambling occurring at 17.1 ± 4.9 min. FAF cells, on the other hand, exhibit overall reduced pSIVA accumulation (Fig. 3*G*), a diminished rate of scrambling (Fig. 3*H*), and, most strikingly, a 20-min delay in the onset of scrambling at 39.9 ± 7.6 min (Fig. 3*I*). Both 16A and mCh-cyto cells show minimal, if any, pSIVA binding (Fig. 3*G*), which strongly correlates with their deficiency in vesiculation. These results demonstrate that not only do cultured

cells require lipid scrambling to successfully generate GPMVs but TMEM16F-dependent lipid scrambling may be required for optimal induction. Furthermore, the timing of scrambling onset appears to be a critical parameter in GPMV formation.

GPMV Generation Requires Calcium Activation of TMEM16F. Experimental evidence from functional and structural studies of TMEM16A (12, 13, 45) and the fungal homolog nhTMEM16 (11) suggests that the calcium-binding site on each monomer subunit is composed of six amino acids found on transmembrane helices 6–8 (TM6–TM8) and is predicted to coordinate two Ca^{2+} ions. These residues are conserved in TMEM16F: N620 and E624 on TM6, E667 and E670 on TM7, and E699 and D703 on TM8 (Fig. 4 *A* and *B*). Of these, only E667 has been confirmed
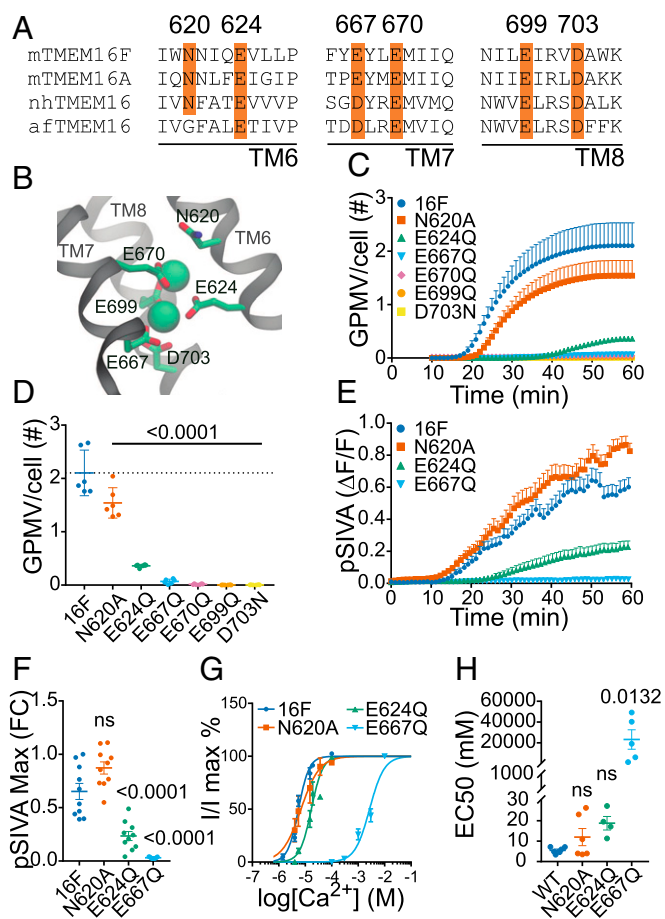
Fig. 4. TMEM16F calcium-binding mutants show deficiency in vesiculation. (A) Amino acid alignment depicting the six predicted calcium-binding residues in TMEM16F: N620 and E624 on TM6, E667 and E670 on TM7, and E699 and D703 on TM8. All acidic residues are conserved among nonscrambling TMEM16A and the fungal TMEM16 homologs nhTMEM16 and afTMEM16. (B) Close-up view of the calcium-binding site in a TMEM16F homology model. Calcium ions are represented as green spheres. (C) Quantification of GPMV generation by HEK cell lines stably expressing TMEM16F-mCherry with mutations in each calcium-binding residue. (D) Scatter dot plot showing the average number of GPMVs produced per cell after 1 h. (E) Quantification of average pSIVA fluorescence normalized to mCherry from time-lapse images. (F) Scatter dot plot showing the maximal pSIVA fluorescence per cell. (G) Electrophysiological recordings showing right shift of Ca^{2+} sensitivity by calcium-binding mutants. (H) Scatter dot plot showing average EC_{50} values for Ca^{2+} gating. Statistical significance was determined for all mutants compared with 16F wild type by one-way ANOVA followed by a Holm–Šídák multiple comparisons test for D and F. Significant differences for EC_{50}s of Ca^{2+} response curves of mutants compared with 16F wild type were determined with Kruskal–Wallis tests followed by Dunn's multiple comparison tests. In F and H, ns indicates not significant.

experimentally in TMEM16F to alter Ca^{2+} sensitivity in current activation (16). We stably expressed TMEM16F-mCherry bearing point mutations in each calcium-binding residue in HEK293 cells to test their role in GPMV generation. Cell lines bearing a charge-neutralizing mutant for four of the five acidic residues (E667Q, E670Q, E699Q, and D703N) fail to vesiculate within 1 h (Fig. 4 C and D), similar to 16A, mCh-cyto, and untransfected HEK293 cells. Cells expressing a charge-neutralizing mutant for the fifth acidic residue (E624Q) demonstrated the capacity to vesiculate but exhibited a considerably diminished response, averaging 0.4 ± 0.03 vesicle per cell, or 18% that of WT 16F. The N620A mutant, on the other hand, led to mild, although statistically significant,

deficiencies in GPMV generation, producing, on average, 1.5 ± 0.3 vesicles per cell, ~70% that of WT 16F.

We next performed live cell imaging with pSIVA to assess whether deficient vesiculation corresponded to defective scrambling activity. Consistent with predictions, cells expressing the vesiculation-dead E667Q mutant did not externalize PS following GPMV treatment, whereas the partially defective E624Q mutant led to a delay in scrambling onset and greatly diminished magnitude of PS externalization (Fig. 4 E and F). Interestingly, cells expressing the N620A mutant showed no indication of scrambling deficiency compared with wild type, instead exhibiting a slightly augmented maximal response, suggesting that their moderate reduction in vesiculation may be due to a mechanism independent of PS translocation. Finally, we tested the channel activity of these calcium-binding mutants and found that E667Q has an EC_{50} at 23.2 ± 9.4 mM, about a 4,000-fold reduction in Ca^{2+} sensitivity compared with that of WT 16F, 5.5 ± 0.6 µM, which is consistent with previously reported data (16). Both N620A and E624Q show moderate right shifts with EC_{50}s of 12.0 ± 4.2 µM and 18.8 ± 3.3 µM, respectively (Fig. 4 G and H), which correlate well with partial reduction of activity in the vesiculation assay.

Mutating Predicted Pore-Lining Residues on TM6 Promotes TMEM16F Activity. Pore-lining residues were identified on TM6 of TMEM16A that, when substituted with alanine, led to a channel prone to activation at lower concentrations of Ca^{2+} (41). We generated mutant constructs to analogous residues in TMEM16F (I612, G615, and K616) with the prediction that they might also accelerate lipid translocation due to heightened Ca^{2+} sensitivity. These residues are not strictly conserved in the extended TMEM16 family and may represent a more specialized function in mammalian TMEM16 proteins. Although the fungal TMEM16 homologs have a hydrophobic phenylalanine at the I612 position, G615 and K616 of TMEM16F are not conserved at all in fungal homologs (Fig. 5A). Since I612 is predicted to contribute bulk and/or hydrophobicity to the putative pore region, in addition to mutating it to alanine, we further substituted it with either valine or threonine, which are similar in bulk but have different hydrophobicity, to distinguish between the two factors. TMEM16A cryo-EM structures suggest that TM6 bends or flexes at G615 (12, 13), which modulates the diameter of the hydrophilic groove that is considered the pore for ion conductance (Fig. 5B). In addition, it has also been suggested that upon Ca^{2+} activation, two calcium-binding residues, N620 and E624, that reside on the lower half of TM6 are recruited to the Ca^{2+} binding pocket, causing TM6 to swing outward, further dilating the pore (12, 13). We expected that alanine mutation of G615 would enforce rigidity upon this predicted hinge region in TM6. Moreover, mouse TMEM16F has an additional glycine at position 614 not found in TMEM16A, so we also mutated it to alanine and generated a double G614A/G615A (GAGA) for analysis. Last, we generated K616 mutants that either neutralized (K616A, K616Q) or reversed the charge (K616E) of this critical residue.

We chemically induced vesiculation in cells stably expressing TMEM16F with these mutations and found that although only the K616 mutants showed an increase in the total number of GPMVs generated (Fig. 5 E and F), all of the activating mutants had accelerated time to onset for GPMV formation (Fig. 5G). Cells expressing the K616E mutant produced the greatest number of vesicles in this study (2.9 ± 0.1 GPMVs per cell) and exhibited the fastest measured time to vesiculation (11.3 ± 0.8 min). The cell lines expressing the other two K616 mutants, K616A and K616Q, followed closely with 2.6 ± 0.1 and 2.5 ± 0.1 GPMVs produced per cell with onset times of 11.8 ± 0.8 min and 15.7 ± 0.8 min, respectively. The I612A mutant had the third fastest GPMV onset time of 14.8 ± 0.6 min (Fig. 5C). I612T retained the activating effect of I612A, with a GPMV onset of 19.9 ± 0.4 min, whereas I612V was slightly slower than WT, with an onset time of 26.7 ± 0.8 min, suggesting that the mechanism
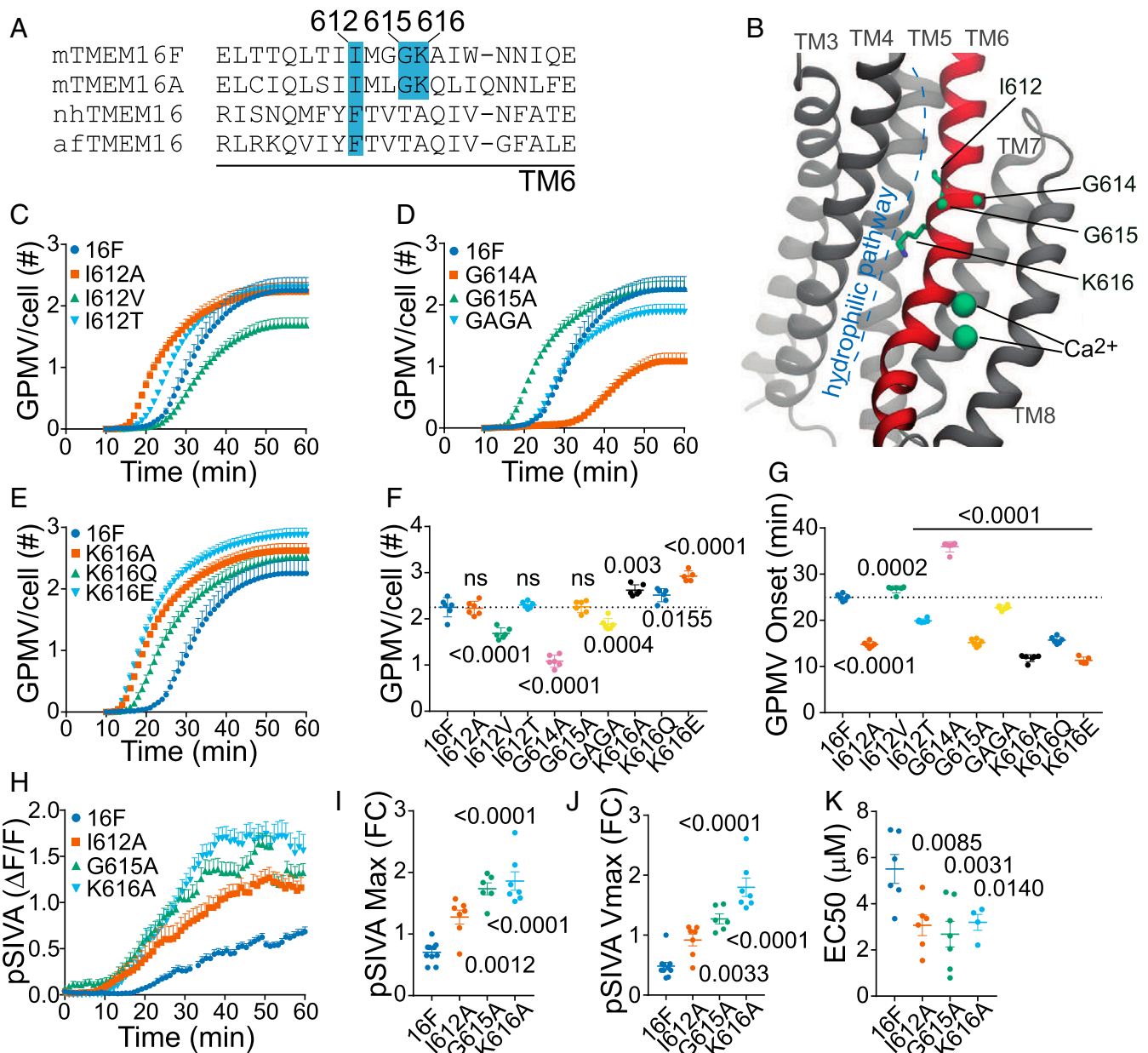
Fig. 5. Activating mutants on TM6 promote GPMV generation. (*A*) Alignment of TM6 helices reveals variations at positions I612, G615, and K616. (*B*) Structural view of TM6 residues within the context of the hydrophilic groove and the calcium-binding site. (*C*) Quantification of GPMV generation for I612 mutants that either eliminates the bulky, hydrophobic side chain (I612A), slightly reduces the hydrophobicity (I612V), or greatly reduces hydrophobicity (I612T). (*D*) Quantification of GPMV generation for alanine mutants that reduce the flexibility of G615 (G615A), neighboring G614 (G614A), or the double G614A/G615A (GAGA) mutant. (*E*) Quantification of GPMV generation for K616 mutants that either neutralize the charge (K616A and K616Q) or reverse the charge (K616E). (*F*) Scatter dot plots showing the average number of GPMVs produced after 1 h of incubation and (*G*) the average time to onset for vesiculation. (*H*) Quantification of pSIVA fluorescence normalized to mCherry from time-lapse images. Scatter dot plots showing (*I*) the maximal pSIVA fluorescence per cell and (*J*) the maximal rate of pSIVA accumulation per cell. (*K*) Scatter dot plot obtained from electrophysiological recordings showing the increase of Ca^{2+} sensitivity by TM6 activating mutants. Statistical significance of all mutants compared with 16F wild type was determined by one-way ANOVA followed by a Holm–Šídák multiple comparisons test for *F*, *G*, *I*, and *J*. Significant differences for EC_{50}s of the Ca^{2+} response curves of mutants compared with 16F wild type were determined with Kruskal–Wallis tests followed by Dunn's multiple comparison tests. In *F* ns indicates not significant.

==**of activation depends on decreasing hydrophobicity rather than reducing steric hindrance.**== Mutation of the first TM6 glycine in mouse TMEM16F (G614A) led to a diminished and delayed vesiculation response, but mutation of the second glycine (G615A), which is conserved in TMEM16A, had an accelerated vesiculation onset time of 15.2 ± 0.8 min, although producing a similar number of total vesicles as wild type (Fig. 5*D*). Interestingly, the double glycine mutant (GAGA) appears to restore WT kinetics with a slight decrease in magnitude. From

these data, we conclude that G615 corresponds to the glycine hinge described for TMEM16A and alanine substitution at this position either accelerates the transition kinetics or stabilizes the straightened helix present when the pore is fully open.

==We found that consistent with our GPMV data, I612A, G615A, and K616A mutants also promoted lipid scrambling (Fig. 5*H*).== These activating effects were apparent in the increase of the maximal amplitude of pSIVA accumulation (Fig. 5*I*) due to an accelerated V_{max} (Fig. 5*J*). We also found that, similar to

TMEM16A (41), these mutations all shift the TMEM16F Ca^{2+} binding curve to the left, with EC_{50}s on average 2–3 µM less than WT (Fig. 5K). However, the EC_{50} values do not recapitulate the trend exhibited by these mutants in the GPMV generation assay, suggesting that heightened sensitivity to Ca^{2+} only partially accounts for increased activity.

Mechanism of Calcium Activation in GPMV Generation. Because both microvesicle production and TMEM16F activation are Ca^{2+}-dependent, we next investigated whether cellular exposure to PFA leads to an intracellular Ca^{2+} rise and whether that might also underlie GPMV generation. To measure Ca^{2+} levels, we loaded cells with green fluorescent Ca^{2+} reporter dye Fluo-5N before chemical induction of vesiculation. Upon inducing GPMV formation, we observed that vesiculation is indeed robustly correlated with a Ca^{2+} rise in cells expressing either WT TMEM16F or the activating K616A mutant, while nonvesiculating cells expressing either mCherry-tagged TMEM16F calcium-binding mutant E667Q or mCh-cyto alone experienced a severely diminished Ca^{2+} response to PFA (Fig. 6 A and B). The onset time for Ca^{2+} rise for 16F cells was observed to be 22.9 ± 0.7 min, which slightly preceded the onset of GPMV generation (Fig. 6C). Furthermore, cells bearing the K616A mutant exhibited accelerated Ca^{2+} increase with a time to onset of 4.3 ± 0.6 min as estimated by curve modeling, although data collected began 10 min posttreatment. Unexpectedly, the magnitude of Ca^{2+} response was decreased compared with WT, perhaps due to weaker overall expression levels of the mutant construct.

Next, we investigated the source of Ca^{2+} required for GPMV generation. Upon repeating the GPMV assay with 16F cells without calcium in the external solution (0Ca), we observed minimal increase in Ca^{2+} levels (Fig. 6D) and no vesiculation (Fig. 6E), indicating that both are dependent on extracellular Ca^{2+}. Interestingly, by titrating increasing amounts of buffer [Ca^{2+}], we observed a concentration-dependent effect on both intracellular Ca^{2+} levels (Fig. 6D) and GPMV generation (Fig. 6E), suggesting

that influx of external Ca^{2+} is required for vesiculation in this assay. We also employed various pharmacological interventions to manipulate the GPMV-associated Ca^{2+} rise. As expected, treatment with intracellular Ca^{2+} chelator BAPTA-AM [1,2-Bis(2-aminophenoxy)ethane-N,N,N′,N′-tetraacetic acid tetrakis(acetoxymethyl ester)] suppressed both intracellular Ca^{2+} (Fig. 6D) and GPMV generation (Fig. 6E), confirming that intracellular Ca^{2+} accumulation is essential for vesiculation. We administered 2-aminoethoxydiphenyl borate (2-APB) concurrently with PFA to block store-operated Ca^{2+} entry in cells undergoing GPMV generation. Conventionally, a low concentration (<10 µM) of 2-APB is used to block store-operated Ca^{2+} entry through inositol trisphosphate receptor inhibition, but at higher doses, 2-APB has been shown to affect Ca^{2+} channels on the plasma membrane (42). In the GPMV assay, 5 µM 2-APB led to partial inhibition of both Ca^{2+} influx, and 50 µM 2-APB completely abolished Ca^{2+} response to PFA treatment (Fig. 6D) and led to a dose-dependent reduction of GPMV production (Fig. 6E). Taken altogether, these experiments reveal a robust linear correlation ($r^2 = 0.9807$) between intracellular [Ca^{2+}] and GPMV response (Fig. 6E). We have further used nanoparticle tracking to analyze extracellular vesicles within physiological size range and found that vesiculation either by calcium ionophore A23187 or with the chemical induction protocol for GPMV formation shows a similar dependence on TMEM16F function (*SI Appendix*, Fig. S4). From these data, we conclude that influx of extracellular Ca^{2+} was primarily responsible for the sustained Ca^{2+} rise experienced by cells undergoing vesiculation and that successful induction of GPMV formation requires accumulation of intracellular calcium and TMEM16F activation.

Discussion

We have developed a robust and quantitative assay for assessing TMEM16F activity by using GPMVs, chemically induced giant vesicles that bud from the plasma membrane. Due to their inherently larger size, they are visible under conventional light
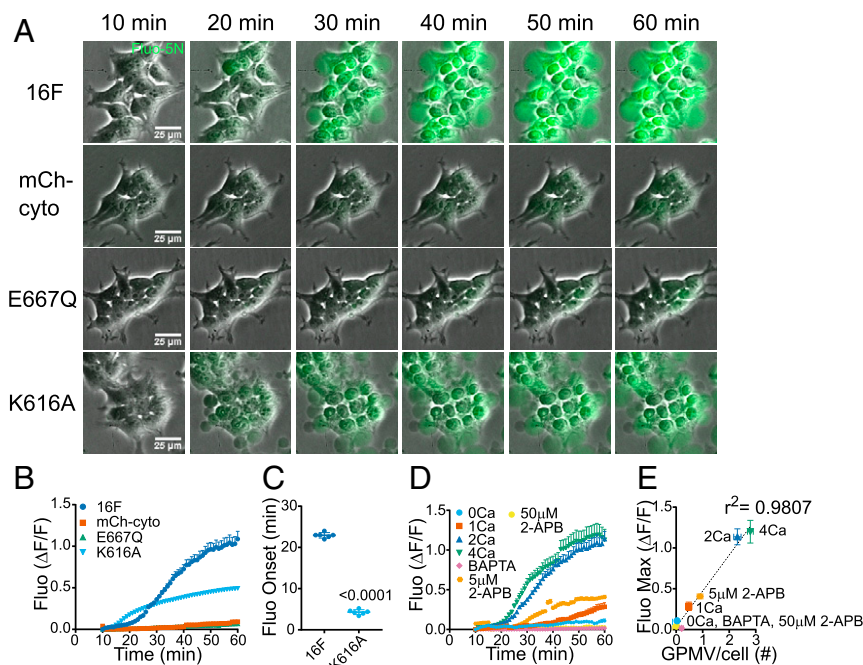
Fig. 6. GPMV treatment induces TMEM16F-dependent intracellular calcium rise. (A) HEK293 cells stably expressing either TMEM16F-mCherry (16F), mCh-cyto, calcium-binding mutant E667Q, or activating mutant K616A are preloaded with calcium reporter dye Fluo-5N (green) and chemically induced to generate GPMVs. (Scale bars: 25 µm.) (B) Quantification of calcium reporter dye over time-lapse series. $P < 0.001$ by unpaired two-tailed t test. (C) Scatter dot plot showing the onset of Ca^{2+} flux. (D) Quantification of calcium reporter dye during GPMV induction under different Ca^{2+} manipulations. (E) Scatterplot showing the correlation between intracellular Ca^{2+} levels and GPMV generation.

microscopy and thus can be monitored in real time. Before our study, it was understood that GPMV generation was a Ca^{2+}-dependent process that produced PS-exposing vesicles which were enriched in cholesterol and sphingolipids (34) and capable of membrane phase separation reminiscent of lipid rafts (35, 36, 43, 44). We further demonstrated that vesiculation was robustly dependent on TMEM16F expression in primary MEF cells in a dose-dependent manner (Fig. 1) and that exogenous expression of TMEM16F-mCherry (16F) protein successfully conferred the ability to produce GPMV to HEK293 cells (Fig. 2). Since under these conditions, untransfected HEK293 cells behave like TMEM16F KO cells, we were therefore able to use it as a platform for probing TMEM16F function.

We found that GPMV generation requires TMEM16F-mediated lipid scrambling activity (Fig. 3 *A* and *B*). Cells that were scrambling-deficient (16A, mCh-cyto, FAF chimera) were either poor vesiculators or unable to vesiculate within the allotted time. The scrambling-competent AFA chimera, however, was able to substitute for TMEM16F expression to produce GPMVs. Interestingly, although AFA cells showed a faster onset of scrambling compared with 16F cells, they yielded only about a third of GPMVs produced by WT 16F. There are several possible scenarios to account for these observations. First, since the AFA construct is primarily composed of the TMEM16A protein sequence with the exception of 35 amino acids from TMEM16F, it is possible that the accelerated onset is due to TMEM16A being more sensitive to Ca^{2+} with an EC$_{50}$ of 0.5–1 μM (12, 45). A second explanation for why AFA cells vesiculated poorly might be that TMEM16F possesses other biophysical characteristics or features important for vesiculation that are absent in TMEM16A and, by extension, the AFA chimera. While activating mutants that promote GPMV vesiculation (i.e., I612A, G615A, and K616A) exhibited enhanced lipid scrambling response (Fig. 5 *H–J*), we also observed that the FAF chimera and the E624Q mutant, which are vesiculation-deficient, are still capable of exposing PS to the extracellular leaflet in response to application of PFA (Figs. 3*F* and 4*E*). This finding perhaps indicates that vesiculation has heightened responsiveness to mild scrambling deficits. Since lipid scrambling appears to be a prerequisite for vesiculation, this makes the GPMV assay a more sensitive, albeit indirect, reporter of scrambling activity. It also supports the hypothesis that TMEM16F has broader functions in extracellular vesicle generation, including, but not limited to, its capacity as a calcium-activated lipid scramblase.

Using the GPMV assay, we experimentally validated the importance of six predicted calcium-binding residues for TMEM16F located on TM6 (N620, E624), TM7 (E667, E670), and TM8 (E699, D703). Four of the five acidic residues (E667Q, E670Q, E699Q, D703N), when replaced with charge-neutralizing amino acids, abolished GPMV generation, while N620A and E624Q exhibited less severe deficiencies (Fig. 4 *C* and *D*). The vesiculation-dead mutant E667Q did not expose PS in response to GPMV treatment, and E624Q displayed severe scrambling deficiencies (Fig. 4 *E* and *F*). N620A, on the other hand, appeared to expose PS as well as or better than WT 16F. Interestingly, E650 in TMEM16A, which corresponds to E624 in TMEM16F, has been shown to coordinate Ca^{2+} in a manner that does not depend on its charge (45), setting TM6 calcium-binding residues apart from the other four. Based on TMEM16A structural studies, we surmised that the calcium-binding residues on TM7 and TM8 might be responsible for coordinating the first Ca^{2+} (12). Following the initial binding, TM6 experiences a conformational change that allows the calcium-binding residues on TM6 to help coordinate the second Ca^{2+} (12, 13, 41). This perhaps indicates that the coordination of the second Ca^{2+} is not an absolute requirement for GPMV formation and may explain why, unlike E667Q, both N620A and E624Q show a moderate increase in their EC$_{50}$ for Ca^{2+} (Fig. 4*H*) and are still capable of calcium-activated lipid scrambling (Fig. 4*E*). In addition, additional asparagines were

implicated in Ca^{2+} binding, which may also explain the mild deficit of N620A in GPMV generation (13).

Quantification of GPMV generation from TMEM16F-overexpressing HEK293 stable cell lines shows a sigmoidal-like curve with a delay in onset of about 24 min, with a duration of 16 min before plateauing around 40 min posttreatment. PS exposure and calcium influx precede the onset of GPMV formation, which has also been shown previously in HeLa-P4 cells (40), and both appear to be required for vesiculation. Given the timing of these events, we suspect that the delay in the onset of GPMV formation is dependent on achieving a certain threshold of intracellular Ca^{2+} for scrambling activation. Furthermore, because the activating mutants on TM6 appear to generate GPMVs for a longer period of time than wild-type TMEM16F (*SI Appendix*, Fig. S3), we speculate that termination of GPMV generation may be due to an intrinsic property of TMEM16F, such as desensitization of TMEM16F due to exposure to high Ca^{2+} (17), rather than a property of the cell such as insufficient lipids for formation of additional vesicles or the equilibration of PS across the bilayer.

Based on our current understanding of Ca^{2+} mobilization under GPMV induction, we believe that cellular exposure to PFA leads to a small Ca^{2+} rise, enough to activate TMEM16F, which in turn induces a sigmoidal-like, sustained Ca^{2+} rise that is dependent on extracellular Ca^{2+}. The exact mechanism for GPMV-associated Ca^{2+} influx is unknown, but it appears to be sensitive to inhibition by 2-APB and tightly correlated with TMEM16F activity. One possibility is that TMEM16F, being a Ca^{2+}-activated cation channel (16), may itself contribute to Ca^{2+} entry. Indeed, researchers have speculated whether cation conductance may be utilized as a counter ion to balance lipid translocation (46), but further investigation would be necessary to test this scenario.

GPMVs are generated using sulfhydryl-blocking reagents such as formaldehyde and *N*-ethylmaleimide (33, 34). In this study, we used 25 mM PFA and 2 mM DTT. Supplementation with DTT was found to allow for a 25% reduction of PFA concentration necessary for GPMV formation by unknown mechanisms, thus limiting potential cellular toxicity (35). On a practical note, our experiments demonstrate that caution may be warranted when subjecting any TMEM16F-expressing cells to chemical fixation. Treatment of our stable HEK293 cell lines with 4% PFA (1.3 M) triggers robust GPMV generation within minutes, which not only distorts cellular morphology but also causes intracellular Ca^{2+} rise, potentially compromising downstream analyses.

In summary, we have demonstrated that chemically induced GPMVs are robustly dependent on TMEM16F-mediated lipid scrambling and can be used as a vesiculation-based assay for TMEM16F activity. The role that lipid scrambling plays in generation of extracellular vesicles is not well understood, although some potential functions include disruption of lipid–protein interactions and modulation of membrane curvature. GPMV generation as a model vesiculation system may prove to be useful in future studies to gain understanding of the precise utility of scrambling in this biological process as well as other potential TMEM16F functions required for extracellular vesiculation.

Materials and Methods

Cell Culture and Cloning.

Primary MEF culture. Embryonic fibroblasts were harvested from mouse embryos E12–E16 from TMEM16F Het × Het matings. Each embryo was processed separately and genotyped at a later date. Tissue was triturated by vigorous pipetting following trypsinization and plated in a six-well plate.
Stable HEK293 cell lines. Wild-type and mutant TMEM16F-mCherry, TMEM16A-mCherry, and cytoplasmic mCherry were subcloned into pENTR1A (Addgene plasmid 17398) and transferred to pLenti CMV Hygro DEST (Addgene plasmid 17454) or pLenti PGK Hygro DEST (Addgene plasmid 19066) using Gateway cloning (Thermo Fisher). Note that the first three amino acids of TMEM16F have been truncated to facilitate expression, but residue numbering is based on full-length reference sequence. pENTR1A no ccDB (w48-1), pLenti CMV Hygro DEST (w117-1), and pLenti PGK Hygro DEST (w530-1) were gifts from

Campeau et al. (47). Lentiviral constructs were cotransfected into HEK293FT cells with packaging plasmids pMD.2G and psPAX2, which were gifts from Didier Trono (Addgene plasmids 12259 and 12260). Lentivirus was harvested from the transfected cells 36–48 h posttransfection, mixed with 8 µg/mL polybrene, and incubated with HEK293 cells to establish stable cell lines under hygromycin selection. All cells (except cytoplasmic mCherry) were verified by microscopy to express mCherry-tagged protein primarily on the plasma membrane at levels comparable to wild-type TMEM16F.

Mass Spectrometry.

Protein identification using LC-MS/MS. WT MEFs, B16F10, and BV2 cells were induced to produce GPMVs using 25 mM PFA and 2 mM DTT in GPMV buffer (10 mM Hepes, 150 mM NaCl, 2 mM $CaCl_2$) for 1.5 h at 37 °C. Following incubation, supernatants from each flask were decanted into conical tubes, centrifuged at $500 \times g$ for 5 min to clear cells and large debris, and ultracentrifuged at $100,000 \times g$ for 30 min to pellet vesicles. Platelets were prepared from WT C57Bl6 mice using previously described methods (16). Purified platelets were resuspended in Ca^{2+}-free Tyrode's Hepes buffer [134 mM NaCl, 12 mM $NaHCO_3$, 2.9 mM KCl, 0.34 mM $NaHPO_4$, 1.0 mM $MgCl_2$, 10 mM Hepes, 0.9% wt/vol dextrose, and 0.35% wt/vol BSA (pH 7.4)] and induced to produce microvesicles using 1 µM calcium ionophore A23187 (Sigma) in the presence of 2 mM $CaCl_2$ for 1 h at 37 °C. Following incubation, platelets were pelleted at $500 \times g$ at room temperature, and the vesicles contained in the supernatant were ultracentrifuged at $100,000 \times g$ for 30 min. Pelleted vesicles were resuspended using 1× LDS (lithium dodecyl sulfate) sample buffer, run on a 4–12% NuPAGE gradient gel (Thermo Fisher), and stained with colloidal Coomassie. In total 19 bands were excised from the colloidal Coomassie-stained SDS gel and subjected to in-gel tryptic digestion. The proteins in the gel bands were reduced with 10 mM DTT (Sigma-Aldrich) at 56 °C for 1 h, followed by alkylation with 55 mM iodoacetamide (Sigma) at room temperature in the dark for 45 min. The samples were then incubated overnight at 37 °C with 100 ng trypsin (sequence grade; Promega). The peptides formed from the digested proteins were then analyzed by online liquid chromatography with tandem mass spectrometry (LC-MS/MS). The LC separation was performed using a nanoACQUITY UPLC system (Waters) on an Easy-Spray PepMap column (75 µm × 15 cm; Thermo Fisher) over a 60-min chromatogram running time. The linear gradient started from 2% buffer B (0.1% formic acid in acetonitrile) and was increased to 30% buffer B at a flow rate of 300 nL/min. The MS/MS analysis was conducted with a LTQ Orbitrap Velos mass spectrometer (Thermo Fisher) and was performed using a top six data-dependent acquisition. The sequence includes one survey scan in the Orbitrap with mass resolution of 30,000 followed by six collision-induced dissociation scans in the linear ion trap. The analytical peak lists were generated from the raw data using in-house software, PAVA (48). The MS/MS data were searched against the UniProt mouse database using an in-house search engine, Protein Prospector (prospector.ucsf.edu/prospector/mshome.htm).

Gene ontology analysis. AmiGO 1.8 (49–51) was used to generate a list of extracellular vesicle-related genes under the category "extracellular exosome" (GO: 0070062), and the MGI identifiers were converted to UniProKB IDs to analyze the enrichment of EV-related proteins in our proteomics experiments.

Western Blotting.

Cultured cells were washed twice in Dulbecco's PBS (DPBS), scraped into 1 mL DPBS, and centrifuged at $1,000 \times g$ for 5 min. Cell pellets were resuspended and lysed in radioimmunoprecipitation assay buffer (50 mM Tris, 150 mM NaCl, 1% Nonidet P-40, 0.5% sodium deoxycholate, 0.1% SDS) with 1 mM PMSF and 1 mM tris(2-carboxyethyl)phosphine. Whole-cell lysate was then diluted in 4× LDS sample buffer (10 µg loaded for Fig. 1*B*, 2 µg for Fig. 2*C*) and resolved on a 4–12% NuPAGE gradient gel, transferred to 0.2 µm nitrocellulose membrane using a semidry blotter, blocked for 1 h in 5% milk in TBST (tris-buffered saline and Tween 20) (20 mM Tris, 150 mM NaCl, 0.1% Tween-20), and incubated overnight in primary antibody in 2% milk in TBST. On the next day, blots were washed three to five times in ddH₂O and once in TBST, incubated with HRP-conjugated secondary antibody, washed three times in TBST, and developed with ECL imaged using a Li-Cor C-digit scanner. Primary antibodies used in this study were 1:500 rabbit polyclonal α-TMEM16F (16), 1:1,000 chicken polyclonal α-mCherry (Abcam), and 1:2,000 mouse monoclonal α-tubulin (Sigma). Secondary antibodies used in this study were 1:20,000 goat anti-rabbit-HRP (Thermo Fisher), 1:20,000 goat anti-chicken-HRP (Thermo Fisher), and 1:20,000 donkey anti-mouse-HRP (Jackson ImmunoResearch).

Microscopy.

Confocal imaging. The 16F- and mCh-cyto-expressing stable HEK293 cells were incubated with lentivirus to express EGFP-PH-PLCδ 36–48 h before imaging. Cells were plated in glass-bottom dishes coated with 1× poly-L-lysine (Sigma) and 1:2,000 Matrigel (Sigma) 2 h before imaging.

GPMV generation assay. In only *SI Appendix,* Fig. S1, preincubation with 1:1,000 Cell Trace CFSE (Thermo Fisher), a nonspecific green fluorescent dye, was used to facilitate visualization. Cultured cells were incubated with NucBlue Live Cell Stain (Thermo Fisher) for 10 min, washed twice in DPBS, and treated with 25 mM PFA/2 mM DTT in GPMV buffer (10 mM Hepes, 150 mM NaCl, 2 mM $CaCl_2$) for live cell imaging on a Nikon-TE2000 Inverted Scope (Nikon Instruments) equipped with a thermostat chamber. Images were acquired once every minute starting 10 min posttreatment for 50 min for a total of 1 h of treatment time. Quantification of the number of GPMVs in each frame was collected using custom software (see *GPMV Quantification* for more detail). Images of nuclear staining were acquired after each experiment and were used to quantify the number of cells in each field for normalization purposes.

pSIVA scrambling assay. Cultured cells were incubated with NucBlue Live Cell Stain for 10 min, washed twice in DPBS, and incubated in calcium-free GPMV buffer (10 mM Hepes, 150 mM NaCl, 0.1 mM EGTA) and 1:200 pSIVA (BioRad). Image acquisition began once PFA/DTT/$CaCl_2$ was added to a final concentration of 25 mM/2 mM/2 mM and terminated after 1 h. Image analysis was carried out on each individual cell using the Nikon Elements software.

Calcium flux assay. Cells were preloaded with 5 µM calcium indicator dye Fluo-5N (Thermo Fisher) for 15 min at 37 °C and washed twice in DPBS before GPMV induction.

Curve Fitting and Statistics.

To calculate the values for V_{max}, time of onset, and duration, we fit the GPMV quantification data, pSIVA imaging data, or Fluo-5N imaging data with the Weibull growth model using GraphPad Prism 7: $Y = YM - (YM - Y0) \cdot \exp(-1(k \cdot x)^g)$. YM is the maximum Y value. $Y0$ is the Y value when x (time) is zero. k is the rate constant. V_{max} is defined as the maximum of the first derivative of this curve, time of onset is the maximum of the second derivative (indicating the maximal acceleration of vesiculation, PS exposure, or calcium rise), and duration is the difference between the maximum and minimum of the second derivative. In all cases, data are represented as mean ± SD except for PS exposure, which is represented as mean ± SEM. Statistical significance was determined by one-way ANOVA followed by a Holm–Šídák multiple comparisons test.

GPMV Quantification.

GPMVs were counted using a custom Python code that employs a combination of a Canny edge detection algorithm (52, 53) and a convolutional neural net designed using lasagne and nolearn (54, 55). The Canny edge detection was combined with a modified Hough transform to detect circles in each image. The convolutional neural net was trained on 32 × 32 pixel images of centered vesicles. Over 1,400 images were selected manually to train the neural net, and these images were not included in the final analysis. To increase the specificity of detection, a particular vesicle was counted only if both the edge detection algorithm and neural net detected the vesicle.

Nanoparticle Tracking Analysis.

Cells were washed twice with DPBS and then incubated with 3 µM calcium ionophore A23187 (Sigma) in calcium-free buffer (10 mM Hepes, 140 mM NaCl, 4 mM KCl, 1 mM $MgCl_2$, 10 mM dextrose, 0.1 mM EGTA) for 5 min at room temperature. Cells were then washed with DPBS twice and incubated in calcium-containing buffer (10 mM Hepes, 140 mM NaCl, 4 mM KCl, 2 mM $CaCl_2$, 1 mM $MgCl_2$, 10 mM dextrose, 0.1 mM EGTA) for 1 h at 37 °C. Supernatants from stimulated cells were collected and centrifuged for $500 \times g$ for 5 min, decanted into fresh tubes, and centrifuged at $2,000 \times g$ for 20 min. Extracellular vesicle concentration (EV mL⁻¹) was determined by nanoparticle tracking analysis (NTA), using a NanoSight LM10 instrument configured with a complementary metal-oxide semiconductor camera and blue 408-nm laser (Malvern Instruments). Videos were recorded five times for each sample, at 60 s each, using a pump flow rate of 40 AU and controlled temperature of 22 °C. All analysis was performed using NTA v3.2 software.

Homology Modeling.

The TMEM16F homology model was generated using both the open nhTMEM16 (PDB 4WIS) and TMEM16A (PDB 5OYB) as templates (11, 13). Sequence alignments were first done for nhTMEM16 and all mammalian TMEM16 sequences using PROMALS3D (56). Using these sequence alignments and template structures, the homology model was generated using MODELER 9.15 (57). A total of 300 models were generated, and the model with the lowest discrete optimized protein energy (58) was selected.

Electrophysiology.

Coverslips with cells were transferred to a recording chamber on a Nikon-TE2000 Inverted Scope (Nikon), and transfection was confirmed with fluorescent microscopy. Patch borosilicate pipets (Sutter Instrument) were pulled from a Sutter P-97 puller with resistances of 2–3 MΩ for inside-out patch recordings. Solutions were puffed to the excised patch using a VC3-8xP pressurized perfusion system (ALA Science). The bath solution contained 145 mM NaCl,

10 mM Hepes, 2 mM CaCl$_2$, 1 mM MgCl$_2$, and 10 mM glucose, pH 7.2 with NaOH. The pipette solution contained 150 mM NaCl, 10 mM Hepes, and 1 mM CaCl$_2$. The membrane patch for inside-out recording was excised in Ca^{2+}-free solution to prevent desensitization (17): 150 mM NaCl, 10 mM Hepes, and 2 mM EGTA. For solutions with Ca^{2+} < 100 μM, Ca^{2+} was added to solutions containing 2 mM hydroxyethylethylenediaminetriacetic acid, and the final concentration was confirmed with Oregon Green BAPTA-5N (Thermo Fisher). The osmolality of each solution was adjusted to 290–310 mOsm/kg. Data were acquired using a Multiclamp 700B amplifier controlled by Clampex 10.2 via Digidata 1440A (Axon Instruments). All experiments were performed at room temperature (22–24 °C). All data were analyzed using pClamp10 (Molecular Devices), OriginLab (OriginLab Corporation), and GraphPad Prism. For the measurement of Ca^{2+} sensitivity, every trace was fit with the Hill equation to generate its respective EC$_{50}$ and H (Hill coefficient). The curves in the figures display the averaged current magnitudes normalized to their respective maximal values (I/I$_{max}$ %). Significant differences for EC$_{50}$s of Ca^{2+} response curves were determined with Kruskal–Wallis tests followed by Dunn's multiple comparison tests. In all cases, data represent mean ± SEM.

1. Contreras F-X, Sánchez-Magraner L, Alonso A, Goñi FM (2010) Transbilayer (flip-flop) lipid motion and lipid scrambling in membranes. *FEBS Lett* 584:1779–1786.
2. van Meer G (2011) Dynamic transbilayer lipid asymmetry. *Cold Spring Harb Perspect Biol* 3:a004671.
3. Pomorski T, Menon AK (2006) Lipid flippases and their biological functions. *Cell Mol Life Sci* 63:2908–2921.
4. Bevers EM, Williamson PL (2010) Phospholipid scramblase: An update. *FEBS Lett* 584: 2724–2730.
5. Sanyal S, Menon AK (2009) Flipping lipids: Why an' what's the reason for? *ACS Chem Biol* 4:895–909.
6. Bevers EM, Williamson PL (2016) Getting to the outer leaflet: Physiology of phosphatidylserine exposure at the plasma membrane. *Physiol Rev* 96:605–645.
7. Lentz BR (2003) Exposure of platelet membrane phosphatidylserine regulates blood coagulation. *Prog Lipid Res* 42:423–438.
8. Zwaal RF, Comfurius P, Bevers EM (2004) Scott syndrome, a bleeding disorder caused by defective scrambling of membrane phospholipids. *Biochim Biophys Acta* 1636: 119–128.
9. Castoldi E, Collins PW, Williamson PL, Bevers EM (2011) Compound heterozygosity for 2 novel TMEM16F mutations in a patient with Scott syndrome. *Blood* 117:4399–4400.
10. Suzuki J, Umeda M, Sims PJ, Nagata S (2010) Calcium-dependent phospholipid scrambling by TMEM16F. *Nature* 468:834–838.
11. Brunner JD, Lim NK, Schenck S, Duerst A, Dutzler R (2014) X-ray structure of a calcium-activated TMEM16 lipid scramblase. *Nature* 516:207–212.
12. Dang S, et al. (2017) Cryo-EM structures of the TMEM16A calcium-activated chloride channel. *Nature* 552:426–429.
13. Paulino C, Kalienkova V, Lam AKM, Neldner Y, Dutzler R (2017) Activation mechanism of the calcium-activated chloride channel TMEM16A revealed by cryo-EM. *Nature* 552:421–425.
14. Pedemonte N, Galietta LJV (2014) Structure and function of TMEM16 proteins (anoctamins). *Physiol Rev* 94:419–459.
15. Picollo A, Malvezzi M, Accardi A (2015) TMEM16 proteins: Unknown structure and confusing functions. *J Mol Biol* 427:94–105.
16. Yang H, et al. (2012) TMEM16F forms a Ca2+-activated cation channel required for lipid scrambling in platelets during blood coagulation. *Cell* 151:111–122.
17. Ye W, et al. (2018) Phosphatidylinositol-(4, 5)-bisphosphate regulates calcium gating of small-conductance cation channel TMEM16F. *Proc Natl Acad Sci USA* 115: E1667–E1674.
18. Fujii T, Sakata A, Nishimura S, Eto K, Nagata S (2015) TMEM16F is required for phosphatidylserine exposure and microparticle release in activated mouse platelets. *Proc Natl Acad Sci USA* 112:12800–12805.
19. Brooks MB, et al. (2015) A TMEM16F point mutation causes an absence of canine platelet TMEM16F and ineffective activation and death-induced phospholipid scrambling. *J Thromb Haemost* 13:2240–2252.
20. Gyobu S, Ishihara K, Suzuki J, Segawa K, Nagata S (2017) Characterization of the scrambling domain of the TMEM16 family. *Proc Natl Acad Sci USA* 114:6274–6279.
21. Suzuki J, et al. (2013) Calcium-dependent phospholipid scramblase activity of TMEM16 protein family members. *J Biol Chem* 288:13305–13316.
22. Malvezzi M, et al. (2013) Ca^{2+}-dependent phospholipid scrambling by a reconstituted TMEM16 ion channel. *Nat Commun* 4:2367.
23. Watanabe R, Sakuragi T, Noji H, Nagata S (2018) Single-molecule analysis of phospholipid scrambling by TMEM16F. *Proc Natl Acad Sci USA* 115:3066–3071.
24. Sims PJ, Wiedmer T, Esmon CT, Weiss HJ, Shattil SJ (1989) Assembly of the platelet prothrombinase complex is linked to vesiculation of the platelet plasma membrane. Studies in Scott syndrome: An isolated defect in platelet procoagulant activity. *J Biol Chem* 264:17049–17057.
25. Ehlen HWA, et al. (2013) Inactivation of anoctamin-6/Tmem16f, a regulator of phosphatidylserine scrambling in osteoblasts, leads to decreased mineral deposition in skeletal tissues. *J Bone Miner Res* 28:246–259.
26. Headland SE, et al. (2015) Neutrophil-derived microvesicles enter cartilage and protect the joint in inflammatory arthritis. *Sci Transl Med* 7:315ra190.
27. György B, et al. (2011) Membrane vesicles, current state-of-the-art: Emerging role of extracellular vesicles. *Cell Mol Life Sci* 68:2667–2688.
28. Raposo G, Stoorvogel W (2013) Extracellular vesicles: Exosomes, microvesicles, and friends. *J Cell Biol* 200:373–383.
29. Chargaff E, West R (1946) The biological significance of the thromboplastic protein of blood. *J Biol Chem* 166:189–197.
30. Wolf P (1967) The nature and significance of platelet products in human plasma. *Br J Haematol* 13:269–288.
31. Choudhuri K, et al. (2014) Polarized release of T-cell-receptor-enriched microvesicles at the immunological synapse. *Nature* 507:118–123.
32. Hu Y, et al. (2016) Scramblase TMEM16F terminates T cell receptor signaling to restrict T cell exhaustion. *J Exp Med* 213:2759–2772.
33. Scott RE (1976) Plasma membrane vesiculation: A new technique for isolation of plasma membranes. *Science* 194:743–745.
34. Scott RE, Perkins RG, Zschunke MA, Hoerl BJ, Maercklein PB (1979) Plasma membrane vesiculation in 3T3 and SV3T3 cells. I. Morphological and biochemical characterization. *J Cell Sci* 35:229–243.
35. Sezgin E, et al. (2012) Elucidating membrane structure and protein behavior using giant plasma membrane vesicles. *Nat Protoc* 7:1042–1051.
36. Baumgart T, et al. (2007) Large-scale fluid/fluid phase separation of proteins and lipids in giant plasma membrane vesicles. *Proc Natl Acad Sci USA* 104:3165–3170.
37. Sengupta P, Hammond A, Holowka D, Baird B (2008) Structural determinants for partitioning of lipids and proteins between coexisting fluid phases in giant plasma membrane vesicles. *Biochim Biophys Acta* 1778:20–32.
38. Yu K, et al. (2015) Identification of a lipid scrambling domain in ANO6/TMEM16F. *eLife* 4:e06901.
39. Wong K, Li X, Ma Y (2006) Paraformaldehyde induces elevation of intracellular calcium and phosphatidylserine externalization in platelets. *Thromb Res* 117:537–542.
40. Keller H, Lorizate M, Schwille P (2009) PI(4,5)P2 degradation promotes the formation of cytoskeleton-free model membrane systems. *ChemPhysChem* 10:2805–2812.
41. Peters CJ, et al. (2018) The sixth transmembrane segment is a major gating component of the TMEM16A calcium-activated chloride channel. *Neuron* 97:1063–1077.e4.
42. Bootman MD, et al. (2002) 2-aminoethoxydiphenyl borate (2-APB) is a reliable blocker of store-operated Ca^{2+} entry but an inconsistent inhibitor of InsP3-induced Ca^{2+} release. *FASEB J* 16:1145–1150.
43. Johnson SA, et al. (2010) Temperature-dependent phase behavior and protein partitioning in giant plasma membrane vesicles. *Biochim Biophys Acta* 1798:1427–1435.
44. Leventhal I, et al. (2009) Cholesterol-dependent phase separation in cell-derived giant plasma-membrane vesicles. *Biochem J* 424:163–167.
45. Tien J, et al. (2014) A comprehensive search for calcium binding sites critical for TMEM16A calcium-activated chloride channel activity. *eLife* 3:e02772.
46. Brunner JD, Schenck S, Dutzler R (2016) Structural basis for phospholipid scrambling in the TMEM16 family. *Curr Opin Struct Biol* 39:61–70.
47. Campeau E, et al. (2009) A versatile viral system for expression and depletion of proteins in mammalian cells. *PLoS One* 4:e6529.
48. Guan S, Price JC, Prusiner SB, Ghaemmaghami S, Burlingame AL (2011) A data processing pipeline for mammalian proteome dynamics studies using stable isotope metabolic labeling. *Mol Cell Proteomics* 10:010728.
49. Ashburner M, et al. (2000) Gene Ontology: Tool for the unification of biology. *Nat Genet* 25:25–29.
50. Carbon S; AmiGO Hub, Web Presence Working Group (2009) AmiGO: Online access to ontology and annotation data. *Bioinformatics* 25:288–289.
51. The Gene Ontology Consortium (2017) Expansion of the Gene Ontology knowledgebase and resources. *Nucleic Acids Res* 45:D331–D338.
52. Canny J (1986) A computational approach to edge detection. *IEEE Trans Pattern Anal Mach Intell* 8:679–698.
53. van der Walt S; scikit-image contributors (2014) scikit-image: Image processing in Python. *PeerJ* 2:e453.
54. Dieleman S, et al. (2015) Lasagne: First release. Zenodo, 10.5281/zenodo.27878.
55. Nouri D (2014) Nolearn: Scikit-learn compatible neural network library. Available at https://github.com/dnouri/nolearn. Accessed February 27, 2018.
56. Pei J, Kim B-H, Grishin NV (2008) PROMALS3D: A tool for multiple protein sequence and structure alignments. *Nucleic Acids Res* 36:2295–2300.
57. Šali A, Blundell TL (1993) Comparative protein modelling by satisfaction of spatial restraints. *J Mol Biol* 234:779–815.
58. Shen MY, Sali A (2006) Statistical potential for assessment and prediction of protein structures. *Protein Sci* 15:2507–2524.